Paper: ASAT-17-087-AF

17th International Conference on
AEROSPACE SCIENCES & AVIATION TECHNOLOGY,
ASAT - 17 – April 11 - 13, 2017, E-Mail: asat@mtc.edu.eg
Military Technical College, Kobry Elkobbah, Cairo, Egypt
Tel: +(202) 24025292 – 24036138, Fax: +(202) 22621908

Numerical Assessment of the Effect of Leading Edge Vortex Breakdown on the Lateral-Directional Derivatives at High Angles of Attack

Ahmed A. Saad*

Abstract: Modern fighters design is characterized by slender wings of sharp leading edges (L.E.) and sharp-sided fore-bodies to provide extremely strong L.E. vortices and thus allowing maneuvering at high angles of attack (AoA), and besides improving stealth characteristics as well. These design features caused remarkable changes in the behavior of lateral-directional derivatives at high AoA. In this paper, the behavior of lateral-directional derivatives at high AoA is investigated for a generic fighter model that employs the sharp-edged trend using computational fluid dynamics (CFD). The study concluded that vortex breakdown is a key-element in deteriorating the lateral-directional stability at high angles of attacks. Also, asymmetric lateral-directional aerodynamic loads at high angles of attack were observed as well. The study also observed higher sensitivity to sideslip at high AoA; a small sideslip angle would destabilize the lateral-directional dynamics. The computed lateral-directional derivatives were utilized to predict the onset value of AoA for wing rock with very good agreement.

Keywords: Computational fluid dynamics, vortical flow theory, high AoA aerodynamics.

Nomenclature

b	Wing span.
C_l	Body-fixed rolling moment coefficient.
C_r	Wing root chord-length.
C_y	Aerodynamic side force coefficient.
g	Gravity acceleration.
H	Pressure altitude.
I_x	Moment of inertia about the body-fixed x-axis.
m	Aircraft mass.
M	Mach number.
p	Non-dimensional body-fixed rolling rate.
Q	Dynamic pressure.
S	Wing surface area.
t	Time
U	Relative wind speed.
V	True air speed.
α	Angle of attack.
φ	Roll angle.

* Lecturer at the Department of Mechatronics, Pyramids High Institute of Engineering & Technology, 6th October City, Cairo, Egypt. ahmsaad64@gmail.com

ξ, η, ζ Computational coordinates: axial, normal, and wrap-around directions respectively.
ρ Air density.
β Sideslip angle.
Λ Wing sweepback angle.

Postscripts

* Non-dimensional parameter. (e.g. $I^*_x = 2I_x/\rho SC_r b^2$, $m^*=2m/\rho SC_r$, $t^* = tU_\infty/C_r$)

Subscripts

b Body axis.
eff Effective.
o Initial conditions.
∞ Free stream.

Second subscript level denotes partial derivative.
Example:

$$C_{l_\beta} \equiv \frac{\partial C_l}{\partial \beta}$$

Abbreviations

AoA	Angle of Attack.
AFRL	Air Force Research Laboratory.
CFD	Computational Fluid Dynamics.
CPU	Central Processing Unit.
L.E.	Leading Edge.
WPAFB	Wright-Patterson Air Force Base.

Introduction

Large amount of aerodynamic databases have been established and utilized in aerodynamic design for traditional configurations (configurations with rounded edges). Recent advanced fighters, such as the F-22, employ slender wings with sharp L.E. and chine-shaped fore-bodies to enhance both the high AoA aerodynamics and stealth characteristics as well. Airframes with sharp-shaped edges have become a trend in modern fighter design. The presence of sharp edges in general fixes the flow separation point and has the ability to generate stronger vortices and consequently higher lift that allow maneuvering at higher AoA. Avoidance of flow separation has been maintained for years as a principal aerodynamic design consideration that it is no longer demanded. The primary advantage of a vortical-type flows is to maintain one type of stable flow over a wide range of attitudes and Mach numbers without the need for flow control devices. Moreover, the associated increase in lift reduces the need for high lift devices. On the other hand, vortical flows are known to have relatively higher drag and unfortunately undesirable impact on the longitudinal and lateral-directional stability at high AoA. In this paper, the author has explored the aerodynamic lateral-directional characteristics for a generic fighter model that employs the sharp-edged trend. In addition, the author provides a consistent explanation of the observed characteristics that should help the design process. The investigation is carried out utilizing an Euler CFD solver and flow visualization tools. The first part of this paper is concerned with the computation of the α-polar and β-polar forces and moments data and roll moment rotary derivatives with physical explanation for the variation of each with AoA. The second part presents the application of a prediction criterion for the onset AoA of wing rock [10], which utilizes the computed derivatives in the first part of this paper.

The predicted onset value of AoA for wing rock was found in good agreement with the model CFD-simulation at the predicted onset that was excited by an initial perturbation in roll. This agreement is implicitly considered a good validation for the computed lateral-directional derivatives at the relevant range of AoA.

Model Geometry and Grid Generation

The utilized model in this study is for a generic fighter model that consists of a tapered conical fore-body with chine-shaped cross-section of 90^o-included angle, and a sharp-edged flat-plate cropped delta wing of 65^o-sweep that is blended to the body and beveled along all edges at 45^o (Fig. 1). The non-dimensional values of mass and moment of inertia about the model longitudinal axis were chosen as ($m^* = 35.3$, $I^*_{xb} = 0.684$). The model shape and mass properties were chosen to approximate those of a modern fighter such as the Mirage 2000 [1], with the wing L.E. and fore-body sides sharpened to meet the objectives of the present study.

The axi-symmetric geometry of the fore-body motivated the utilization of a C-O grid topology (Fig. 2). The outer boundaries of the physical domain consist of a cylinder of three-characteristic lengths long connected to a hemisphere of radius 1.5 characteristic lengths (Fig. 3). The relatively small dimension of the outer domain was treated via the implementation of the characteristic boundary conditions [2] to reduce the total number of grid points and thus reducing the anticipated computational cost of the study. Two grids of different dimensions were developed, a baseline grid of dimensions 79x35x65 in the axial, normal, and wrap-around directions respectively and a fine grid of dimensions 117x53x97. The non-dimensional time step defined as: $\Delta t^* = \Delta t\, U_\infty / C_r$ is given by 0.002.

Code Formulation

The Unsteady Euler equations are coupled with the rigid-body dynamic equations in roll, side, and normal DoF to simulate wing rock motion. It is well-known that the unsteady Euler equations are capable of capturing both, the primary vortices and vortex breakdown as a consequence of the inherent dissipation associated with the numerical algorithm. However, adequate application of the Euler equations is limited to flows over configurations with sharp edges, where the location of the separation point is kept fixed at the edge-apex. The Unsteady Euler Equations are numerically solved using the implicit, approximately-factored finite difference scheme of Beam and Warming [3] in the diagonalized form of Pulliam and Chaussee [4]. The equations were differenced using second-order accurate central difference for the temporal and spatial derivatives. A blend of nonlinear second and fourth order spectral damping was employed. The boundary conditions were treated implicitly via sub-iterative procedure, which also helps to relax the stability boundaries imposed on the computational scheme due to the triple factorization. The FDL3DI flow solver, provided by the AFRL (WPAFB), incorporates the previously described numerical scheme. The nondimensional rigid-body equations were differenced in time using second-order accurate backward difference. The rigid-body equations were explicitly coupled with the flow governing equations. The sub-iteration algorithm was extended to work simultaneously on both of the coupled set of equations. For each time step, the algorithm sub-iterates on the two sets of equations until their solutions reach equilibrium. The implementation of sub-iterations synchronizes the solutions of the coupled set of equations, and hence overcomes the inherent time lag in the explicit solution. The incorporation of the rigid-body dynamics in the FDL3DI has led to the modified version of the code MFDL3DI [5]. For more details on the equations and boundary conditions, the reader is encouraged to refer to [5].

Verification Analysis

For verification purposes, the computed lift coefficient at different AoA has been compared with wind tunnel measurements that have been conducted on a similar model at NASA Langley [6]. The geometrical data for the two models and the test flow conditions are found in Table 1.

The experimental data for the lift coefficient was corrected to match the 65°-sweep of the present model utilizing an analytical method that predicts the low-speed lift coefficient for sharp-edged delta wings [7]. The numerical experiments in this study were performed at free stream Mach number M=0.4 (i.e. in the incompressible range of low speed aerodynamics).

Fig. 4 depicts the values of lift coefficient for the experimental, baseline grid, and fine grid for angles of attack 15°, 20°, 25°, 30°, and 35°. The computed values were found in good agreement with the experimental data, especially at high AoA. At α=35°, the baseline-grid solution for lift coefficient is approximately 8% lower than the experimental value, and 3% lower than the value for the fine-grid solution. Also, vortex breakdown locations for the two models were found in good agreement; the experimental model experiences breakdown first at α=25° [6], while the present model at α=30°. Accounting for the 5°-increase in sweep for the delta wing of the present model over the experimental model, the predicted onset of vortex breakdown looks very satisfactory. The fine grid was used in the rest of the numerical experiments in this study.

Lateral-Directional Aerodynamic and Stability Characteristics

In this section, the previously discussed code (section 3) has been utilized to compute the α-polar and β-polar force and moment characteristics at M_∞=0.4. Fig. 5 depicts the α-polar data for β=0, which demonstrates a maximum lift coefficient of approximately 1.18 that occurs at α=33° (Fig. 5-a). The lift curve looks qualitatively similar to the lift curve of traditional configurations (configurations with wings of rounded L.E. and smooth sided fore-bodies). However, the stall of lift beyond the value of α_{stall} in this case is caused by the onset of vortex breakdown and not by the onset of boundary layer separation. Fig. 6 demonstrates the onset of vortex breakdown on the wing upper surface at α=33° evidenced by zero axial velocity at the vortex cores. The flow over delta wings with sharp L.E. is well known to separate over the L.E. at small angles of attack and as a consequence generates the L.E. spiral vortices (see Fig. 7). It is noted in Fig. 5 (b) and (c) that the side force and rolling moment have nonzero values at high angles of attack, even if the model and free stream conditions are perfectly symmetric. This unique feature of configurations with chine-shaped fore-bodies has been recently observed experimentally [6] and computationally [8]. It must be noted that the observed asymmetries in side force and rolling moment for this model are considered relatively mild. This is due to the relatively large chine angle (90°), which induces week vortices in contrast with fore-bodies of small chine angles (see Fig. 8).

The variation of rolling moment with sideslip angle, for moderate angles of attack ($\alpha \leq 25°$), shows stable rolling moment (negative slope) over a wide range of sideslip angles (Fig. 9 (a)). The generation of rolling moment in vortical flow aerodynamics comes from the asymmetric vortex shedding and/or breakdown on the two wing sides. As shown in Fig. 10, the sideslip angle causes the vortex on the windward side to diffuse and move inboard and the vortex on the leeward side to bound and move outboard. As a result, a difference in lift on the two wing sides is originated and consequently generates the observed rolling moment. In addition, the sideslip promotes vortex breakdown on the windward side and delays it on the leeward side. This feature is related to the reduction in the effective sweep-angle on the windward side versus the increase in the effective sweep on the leeward side (see equation (1)). The increase of the sweep angle is known to delay vortex breakdown and vice-versa [9]. The nice behavior of the

rolling moment over a wide range of sideslip angles for ($\alpha \leq 25^o$) is due to the fact that vortex breakdown has not as yet occurred over this range of angles of attack and sideslip. Fig. 11 shows no evidence of negative axial velocity on the upper wing surface for $\alpha=25^o$ and $\beta=10^o$ and hence no vortex breakdown. At $\alpha=30^o$ and 32^o, vortex breakdown was observed just downstream of the wing trailing edge at zero sideslip. So, at $\alpha=30^o$, a sideslip angle of 4^o caused the breakdown axial location to propagates upstream on the windward side and destabilizes the rolling moment curve (see Fig. 9-b). Similarly, at $\alpha=32^o$, a 2^o-sideslip caused the breakdown axial location to move upstream on the windward side and again destabilizes the rolling moment curve (see Fig. 9-b). At $\alpha=35^o$, for which vortex breakdown is already observed on the wing upper surface at zero sideslip, the rolling moment curve slope shows unstable dihedral derivative (C_{l_β}) even at symmetric flow condition ($\beta=0^o$).

$$\Lambda_{eff} = \Lambda \pm |\beta| \quad (1)$$

The "+" sign is for the leeward side and the "–" sign for the windward side.

The side force curve (Fig. 12) shows undesirable behavior, a negative slope of the side force curve over the whole range of angles of attack, especially at the origin, should result in some sort of adverse sideslip motion. This behavior is obviously due to the absence of the vertical tail. Also, it was noticed that the onset of vortex breakdown at higher sideslip angles has a desired effect on the side force curve (see Fig. 12-b).

Roll rotary experiments have been conducted for the purpose to compute the damping-in-roll derivative (C_{l_p}). Figure 13 depicts the variation in rolling moment coefficient for the whole range of the tested angles of attack at two roll rates ($p=3\pi/4$ and π [s^{-1}]). The roll stiffness (C_{l_φ}) is shown stable (negative) over the whole range of roll angles for moderate angles of attack ($\alpha \leq 32^o$). Away from the transition region, the roll stiffness is negative at the origin ($\varphi=0$) for the whole range of angles of attack. For $\alpha \geq 35^o$, the onset of vortex breakdown destabilizes the roll stiffness at small roll angles (see Fig. 13 for $\alpha=35^o$, and 40^o). It is known that the body-axis roll induces sideslip due to the kinematic interchange of the angle of attack and sideslip (see equation (2)). So, as the wing rolls about its longitudinal axis, it is effectively in a sideslip flow condition.

$$\beta(\varphi) = \tan^{-1}(\tan \alpha_o \sin \varphi) \quad (2)$$

The previously discussed aerodynamic force and moment data were utilized to compute the following stability derivatives: C_{l_β}, C_{y_β} *and* C_{l_p} at the origin ($\alpha = \alpha_o$, $\beta = 0$, $\varphi = 0$, and $p = 0$). The first two derivatives, C_{l_β} *and* C_{y_β}, are computed using $2^{nd.}$-order accurate central difference from the data at β =-2^o and 2^o. The damping-in-roll derivative (C_{l_p}) was computed using $1^{st.}$-order accurate forward difference from the data at ($p=3\pi/4$ and π). The variation of the computed derivatives with angle of attack is depicted in figures 14, 15, 16. The dihedral derivative (Fig. 14) becomes destabilizing with the onset of vortex breakdown at $\alpha=33^o$, while the C_{y_β} derivative (Fig. 15) becomes stabilizing with vortex breakdown. The damping-in-roll derivative (Fig. 16) experiences strong nonlinear effects at high angles of attack, and becomes destabilizing (positive) at very high incidences ($\alpha \geq 40^o$), which would indicate a likely roll departure.

Prediction of Wing Rock Onset Based Upon the Lateral-Directional Stability Derivatives

The criterion that predicts the onset angle of attack for which the wing rock is triggered [10] is given in final form as:

$$X_{\Phi} = A\left\{\left[\frac{g}{KV_o}Cos(\alpha_o)+\frac{bA}{2V_oK}Sin(\alpha_o)C_{l_p}\right]C_{l_\beta}-C_{y_\beta}C_{l_p}^{2}\right\} \qquad (3)$$

The sufficient and necessary conditions for ($\alpha_o = \alpha_{onset}$) are:

- $X_\phi(\alpha_{onset}) = 0$, and $a_2(\alpha_{onset}) > 0$.
- $dX_\phi/d\alpha\,|_{\alpha=\alpha_o} = \geq 0$.

where:

$$A = \frac{Q_o\, S\, b}{I_x}$$

$$a_2 = A\left[\left(\frac{\rho\, S\, b}{4\, m}\right)\left(C_{y_\beta}C_{l_p}\right)-C_{l_\beta}Sin(\alpha_\circ)\right]$$

$$K = \frac{\rho^2 S^2 b^3 V_o}{16\, m\, I_x}$$

The trigger parameter, X_φ, computed for different angles of attack from the data in figures 14-16 is shown in Fig. 17. Only point number (2) on the X_φ-graph satisfies the conditions of the onset criterion. The predicted value of the onset angle of attack corresponding to point (2) is $\alpha_o = 40.1^o$. The computational simulation in three DoF: roll, sideslip, and normal direction is conducted using the developed code previously discussed. The wing rock oscillation is triggered by initial perturbation in roll rate from a steady level flight condition at (M = 0.4, H = 2000 [m]). The computational simulation at $\alpha = 40^o$ shows a limit cycle oscillation of 8^o peak-to-peak amplitude in roll angle (see Fig. 18), which is in good agreement with the predicted value of the onset AoA ($\alpha_o = 40.1^o$). Simulations were conducted for $\alpha = 35^o$ and 38^o to verify the results and no limit cycle has been observed for both (see Fig. 19). Also, the study verifies the author's conclusion quoted in [10] that when the value of the C_{l_β}-derivative goes to zero (not the roll stiffness C_{l_φ}, which remains stable) wing rock onset occurs (see Fig. 14). This indicates that a quick and relatively inexpensive computation to predict wing rock onset is to calculate the C_{l_β}-derivative only versus the high computational cost to detect the onset value by repeating multi-cycle simulations such as those depicted in figures 18 & 19.

Conclusions and Recommendations

A computational study investigated the impact of the wing sharp L.E. and the fore-body sharp side edges on the lateral-directional stability of a generic fighter configuration. It was found that the onset of vortex breakdown is a key-element that deteriorates the lateral-directional stability at high angles of attack. The unsteadiness of the vortex breakdown locations on the two wing-halves at high angles of attack was found to cause asymmetric aerodynamic loads while flying in symmetric flight conditions. Sideslip was found to greatly aggravate the asymmetric loads due to the vortical flow nature over these configurations. A combination of high angle of attack and small sideslip angle was found to destabilize the lateral-directional stability derivatives. The associated asymmetric loads are believed to be the direct causes of the

observed lateral dynamic instability problems such as wing rock. The computed stability derivatives were utilized to predict the onset of wing rock using a simple analytical criterion with good agreement for validation purposes that was proved to predict the onset in very good agreement with the CFD simulations.

The study recommends maintaining a burst-free vortical flow over the entire flight envelope in the aerodynamic design of configurations with sharp-sided fore-bodies, which can be achieved by blowing air on the wing upper surface to delay vortex burst. This design consideration resembles the classical concept of maintaining a separation-free flow on traditional configurations. Also, it is recommended to utilize Euler solvers to simulate flow over sharp-edged configurations, which has proved to provide low cost but accurate computational tool. The study recommends scheduling the lateral-directional gains of the stability augmentation system (SAS) based upon the variations in lateral-directional derivatives at high AoA.

References

1. Jackson, P. J. (Ed.), "*Jane's All the World's Aircraft (1999-2000),"* Franklin Watts, New York, 1999.
2. Whitfield, David L., "Three-Dimensional Unsteady Euler Equation Solutions Using Flux Vector Splitting," Printed Notes for a Short Course on Numerical Grid Generation, Mississippi State University, Mississippi State, MS, June 1984.
3. Beam, R. M. and Warming R. F., "An Implicit Factored Scheme for the Compressible Navier-Stokes Equations," *AIAA Journal*, Vol. 16, No. 4, 1978, pp. 393-402.
4. Pulliam, T. H. and Chaussee D. S., "A Diagonal Form of an Implicit Approximate-Factorization Algorithm," *Journal of Computational Physics*, Vol. 39, No. 2, 1981, pp. 347-363.
5. Saad, Ahmed A., and Brad S. Liebst, Ray E. Gordnier, "*Fluid Mechanism of Wing Rock for Configurations with Chine-Shaped Fore-bodies,*" Journal of Aerospace Engineering, Vol. 15, No. 4, October 2002, pp. 125-135.
6. Hall, R. M., "Impact of Fuselage Cross Section on the Stability of a Generic Fighter," AIAA Paper 98-2725, 1998.
7. Polhamus, E. C., "Predictions of Vortex-Lift Characteristics by a Leading-Edge Suction Analogy," *J. Aircraft,* Vol. 8, No. 4, 1971, pp. 193-199.
8. Ravi, R., and Mason, W. H., "A Computational Study on Directional Stability of Chine-Shaped Fore-bodies at High-α," AIAA Paper 92-0030, Jan. 1992.
9. Pelletier, A., and Nelson, Robert C., "Prediction of Vortex Breakdown Location on a Banked Delta Wing," *J. Aircraft*, Vol. 37, No. 4, 2000, pp. 738:740.
10. Saad, Ahmed A. and Liebst Brad S. "An Analytical Criterion for the Prediction and Analysis of Wing Rock Onset," *AIAA Paper 99-4099* (August 1999).
11. Guckenheimer, J., and Holmes, P. Nonlinear Oscillations, Dynamical Systems, and Bifurcations of Vector Fields. New York: Springer-Verlag, 1983.
12. Kinard, Tim A., Harris, Brenda W., and Raj Pradeep, "An Assessment of Viscous Effects in Computational Simulation of Benign and Burst Vortex Flows on Generic Fighter Model Wind-Tunnel Models Using TEAM Code," NASA Contractor Report, NASA-CR-4650, March 1995.

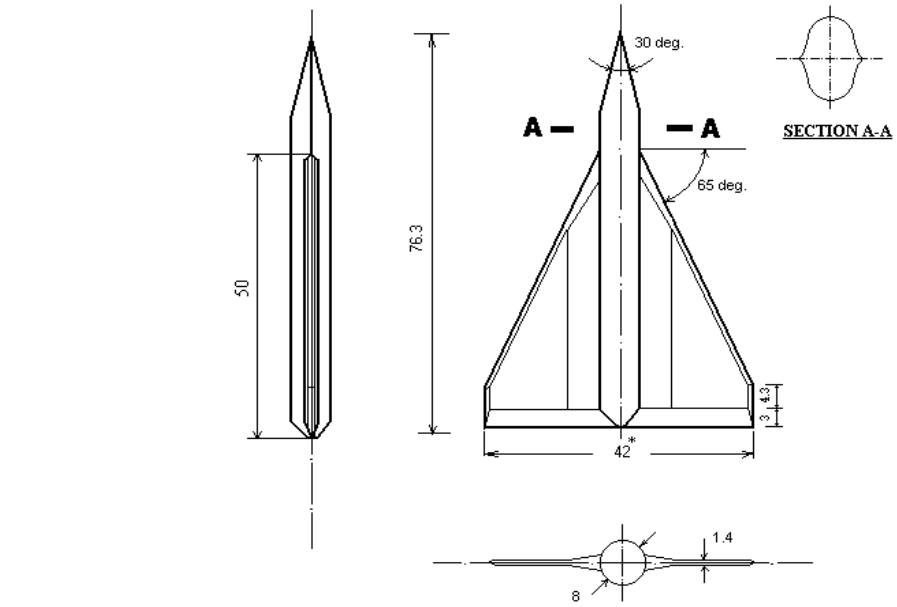

* All dimensions are in Cm, unless otherwise stated.

(a) Three-view drawing for the generic fighter model.

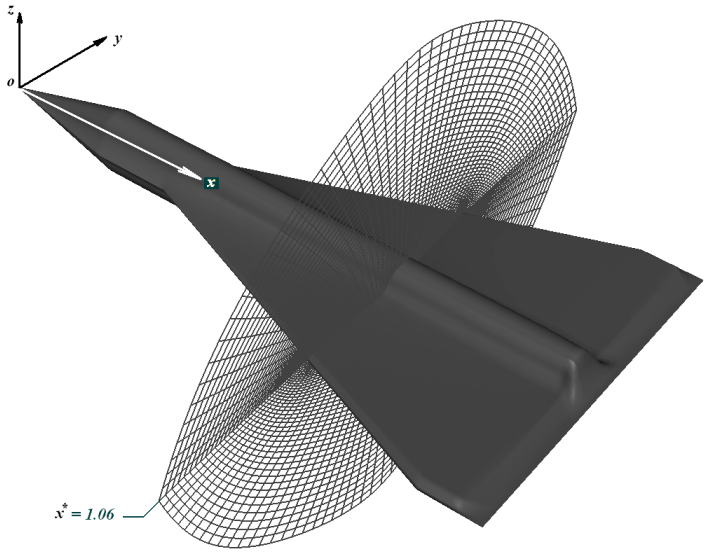

(b) Three-dimensional view for the model.

Fig. 1. Model geometry

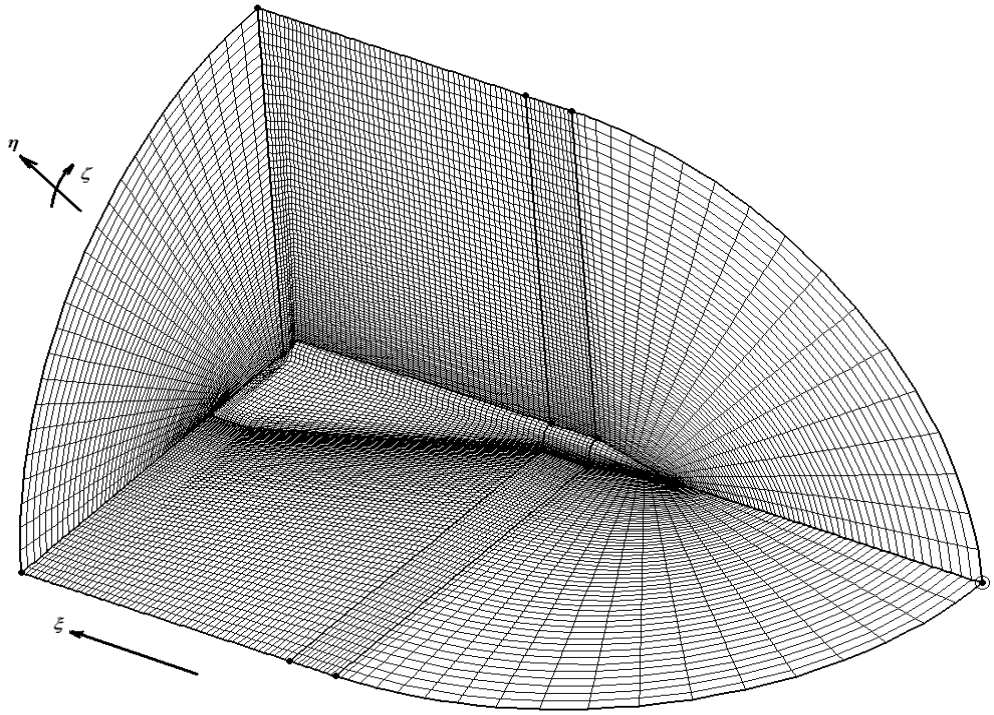

Fig. 2. Section in the wing-body mesh demonstrates the topology.

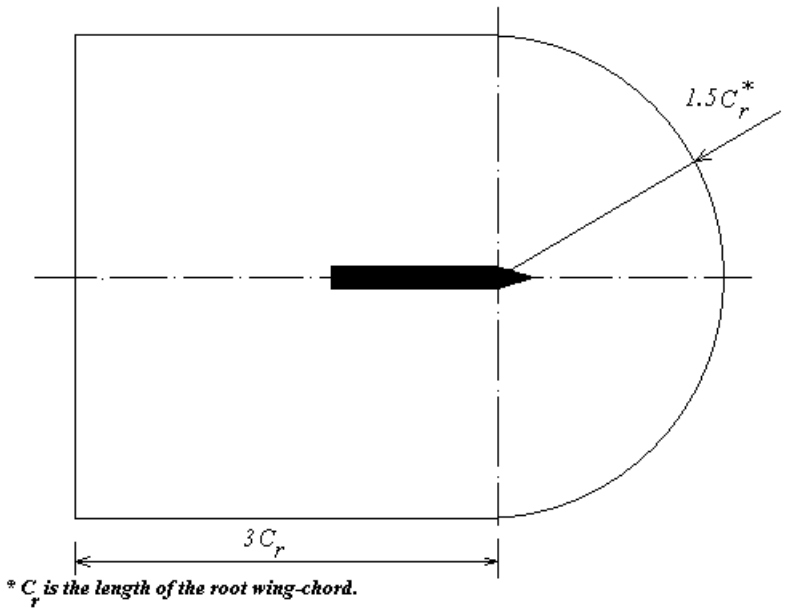

Fig. 3. Physical domain boundaries

Table 1 Experimental and computational model data

	Experimental study [10]	Present numerical study
I- Model Geometry		
- Wing plane-form	Cropped delta	Cropped delta
- Wing sweep	60^o	65^o
- Wing L.E.	Sharp	Sharp
- Wing airfoil	NACA 65-005	
- Forebody cross-section	Chine	Flat-plate
- Chine-angle	100^o	90^o
- Loft above chine*	0.75*	1.2*
- Loft below chine*	0.5*	1.2*
II- Flow conditions		
- Mach No.	0.4	0.4
- Re**	2.67×10^6	2.27×10^6

* Normalized by the local fuselage half width.
** Based on the wing mean aerodynamic chord.

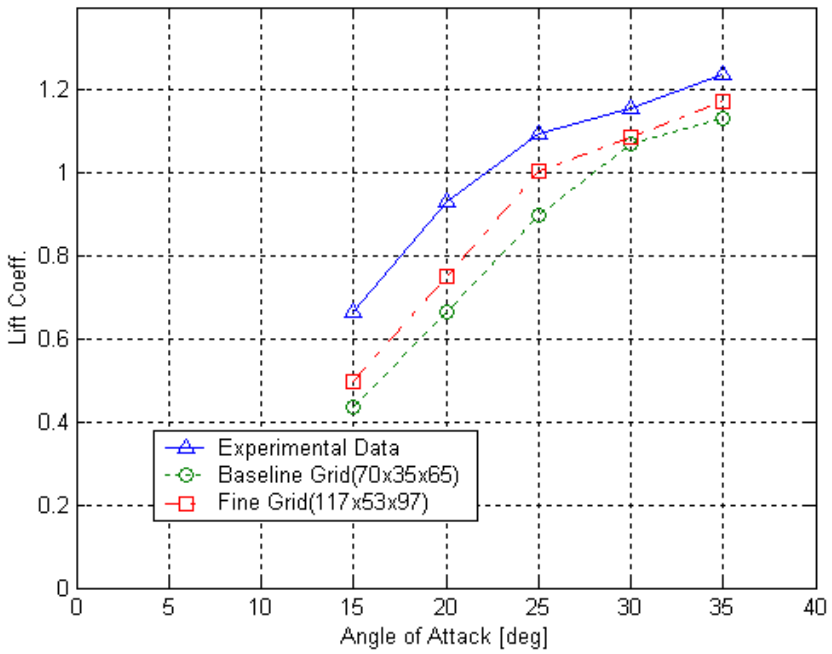

Fig. 4. Comparison between the measured and computed values of lift coefficient for different angles of attack

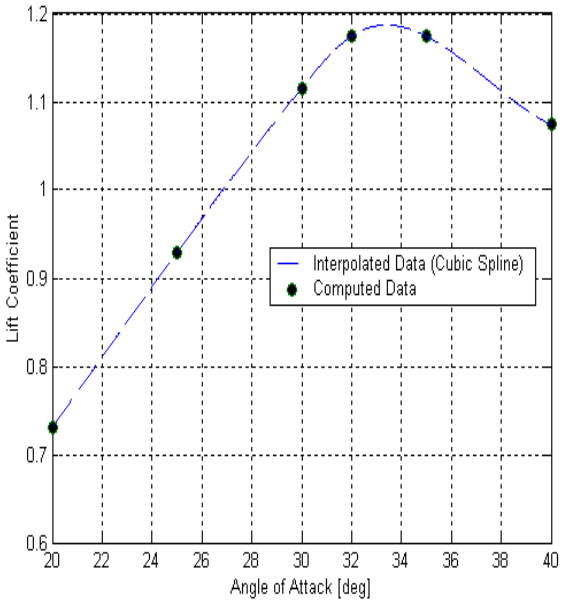

Lift curve

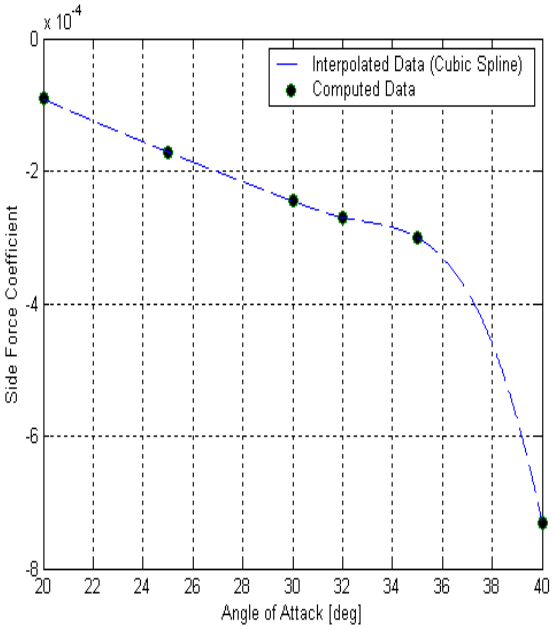

Side force curve

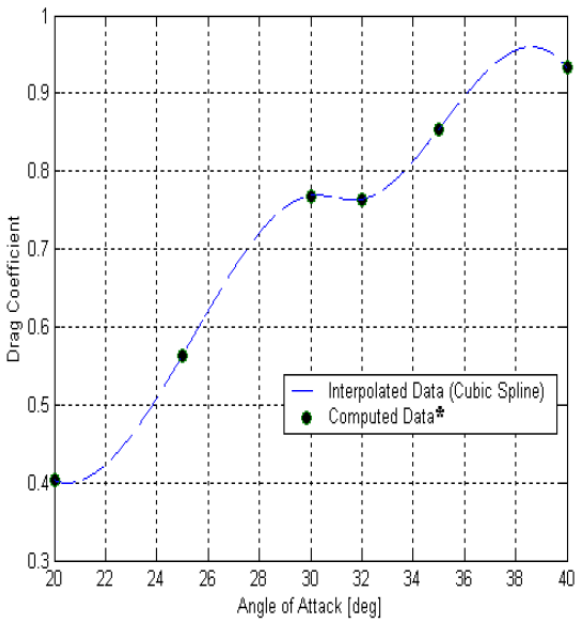

Drag curve

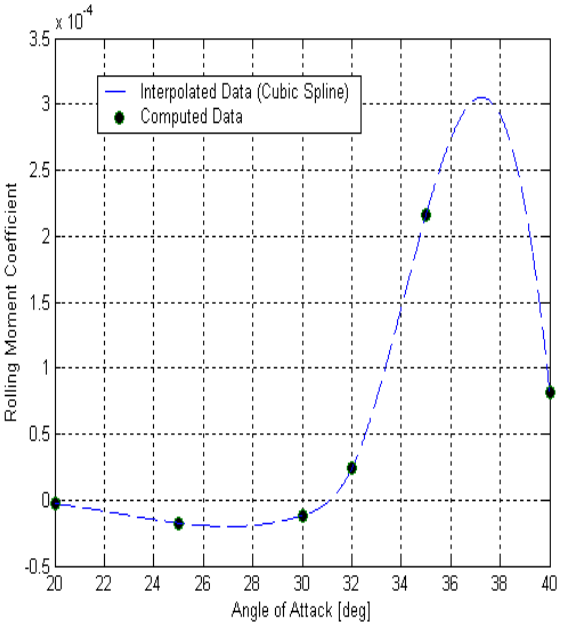

Rolling moment curve

Fig. 5. Force and moment data for β =0

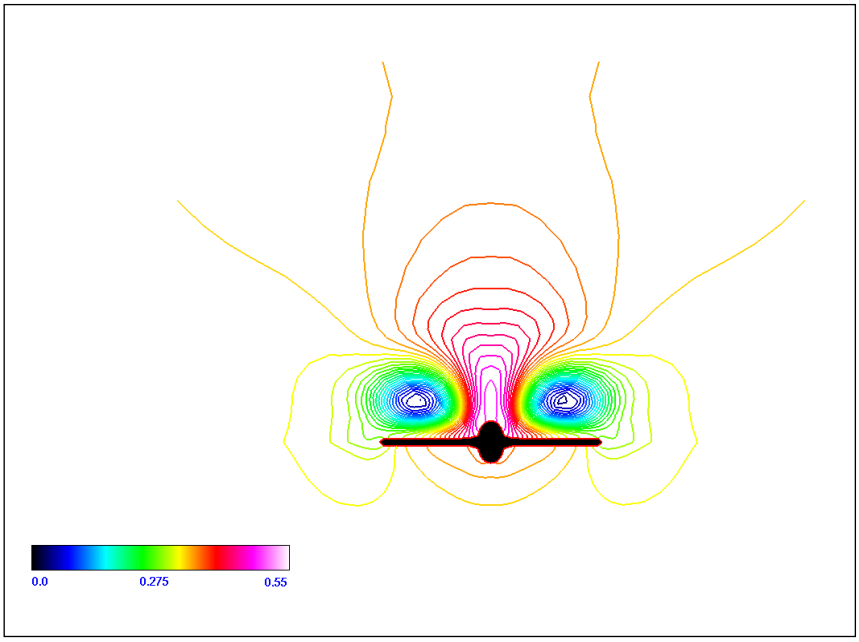

Fig. 6. Non-dimensional axial velocity contours at $\alpha=33^{o}$ and $\beta=0^{o}$ for a wing section at $x^{*}=1.4$

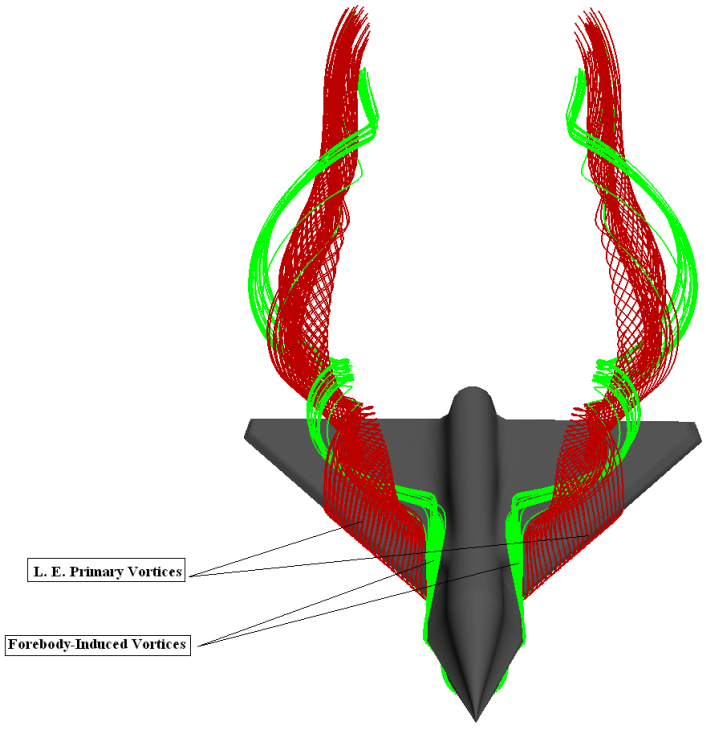

Fig. 7. Fore-body and leading-edge vortices at $\alpha = 25^{o}$ (fine grid)

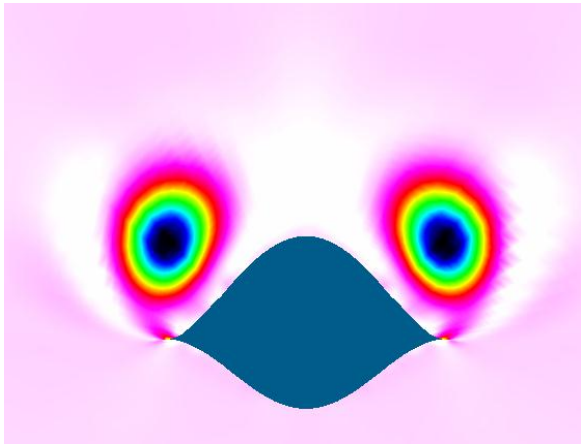

(a) Chine angle = 30º

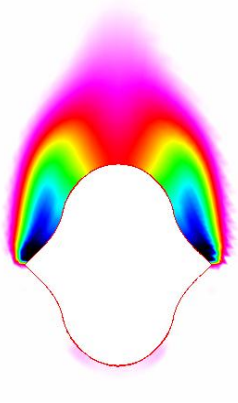

(b) Chine angle = 90º

Fig. 8. Forebody-induced vortices at α=35º visualized by stagnation pressure distribution (fine grid)

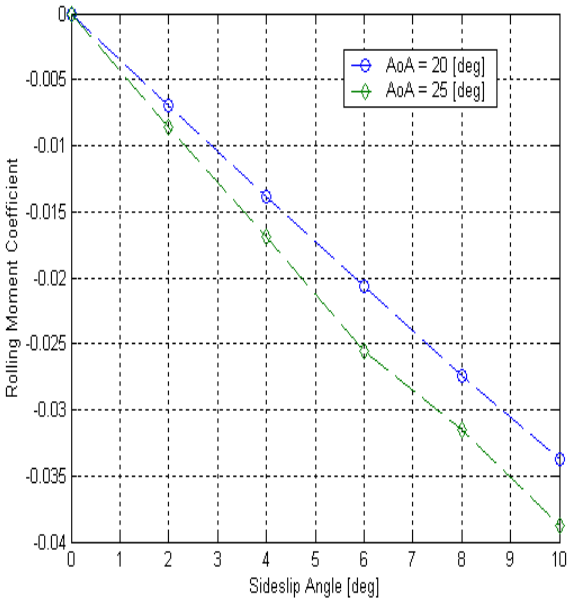

(a)

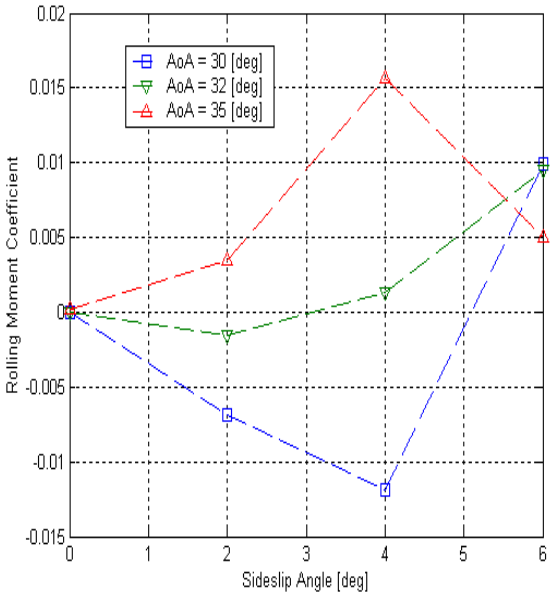

(b)

Fig. 9. Rolling moment coefficient characteristics for different β

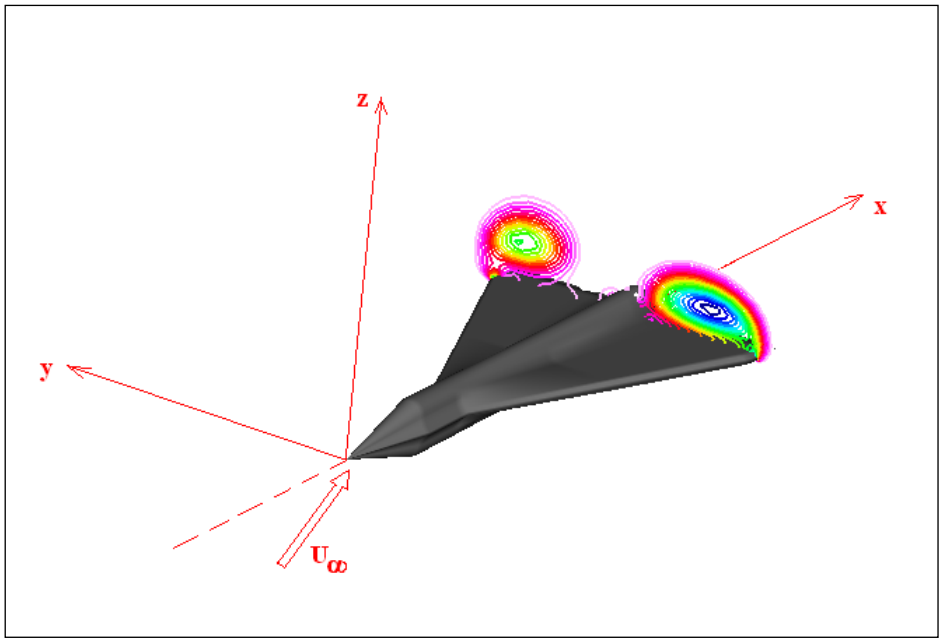

Fig. 10. Vortex structure at $\alpha=25^{o}$ and $\beta=10^{o}$ visualized by stagnation pressure contours

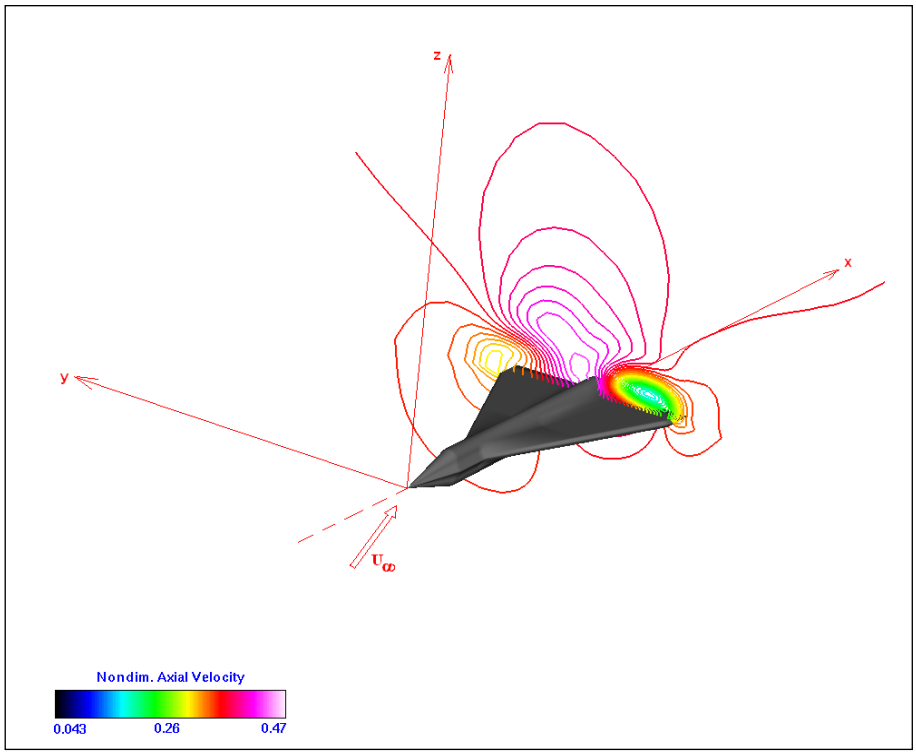

Fig. 11. Non-dimensional axial velocity contours at $\alpha=25^{o}$ and $\beta=10^{o}$

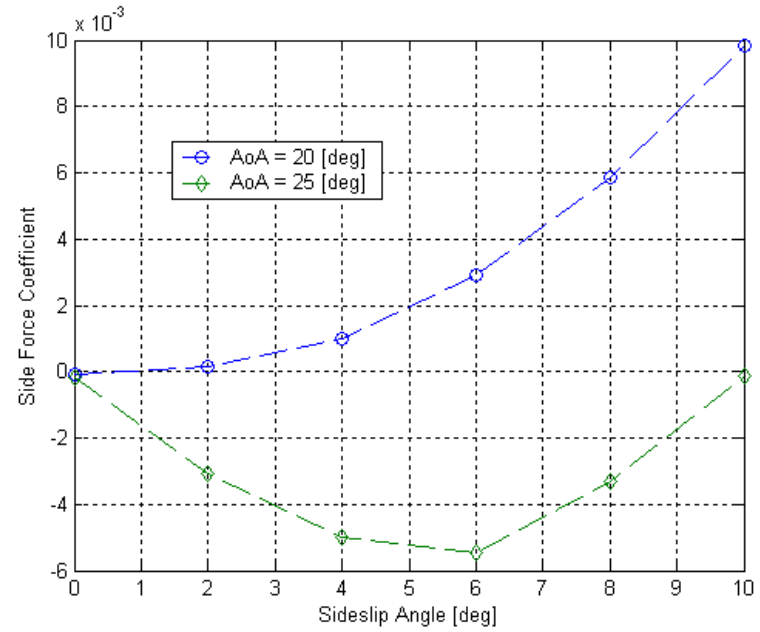

(a)

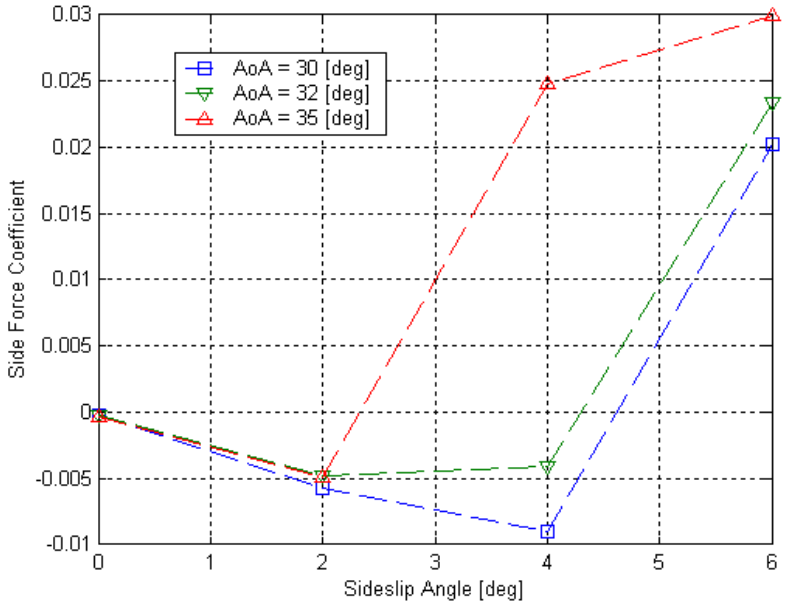

(b)

Fig. 12. Side force coefficient characteristics for different β

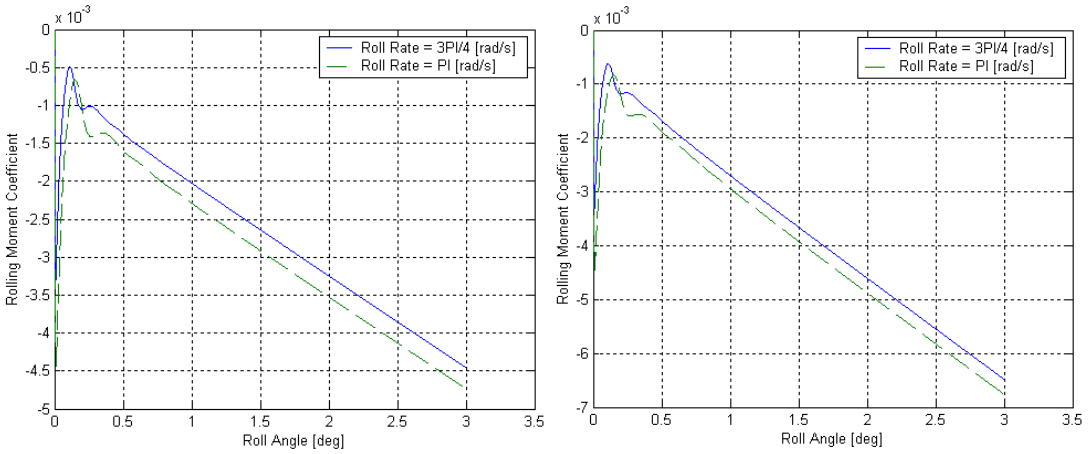

α = 20º

α = 25º

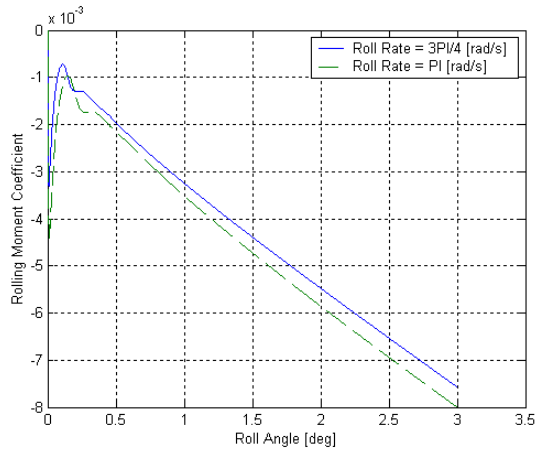

α = 30º

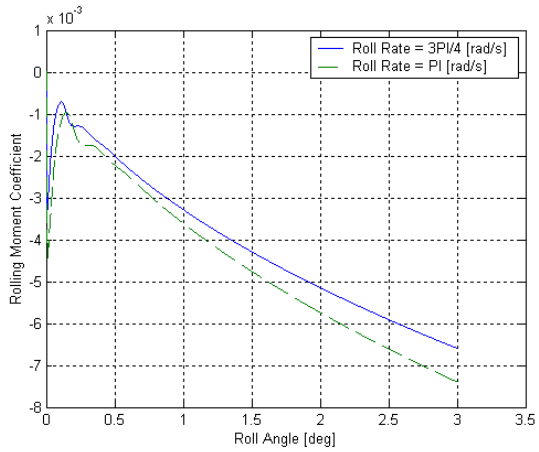

α = 32º

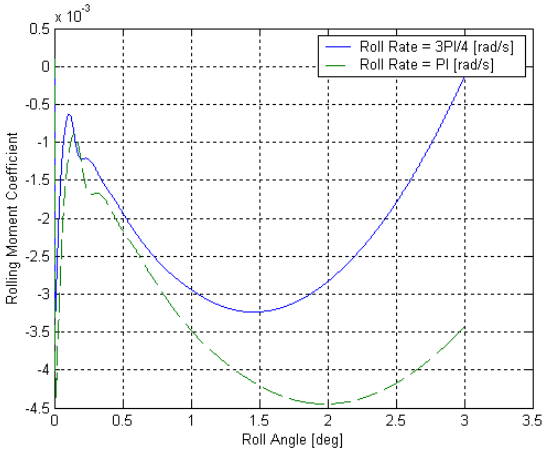

α = 35º

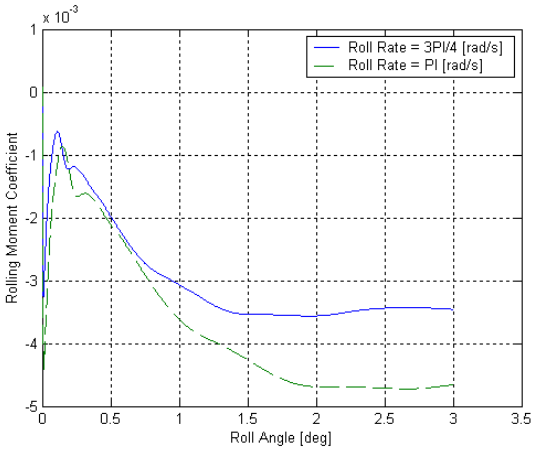

α = 40º

Fig. 13. Variation of the rolling moment coefficient during forced-roll for different α

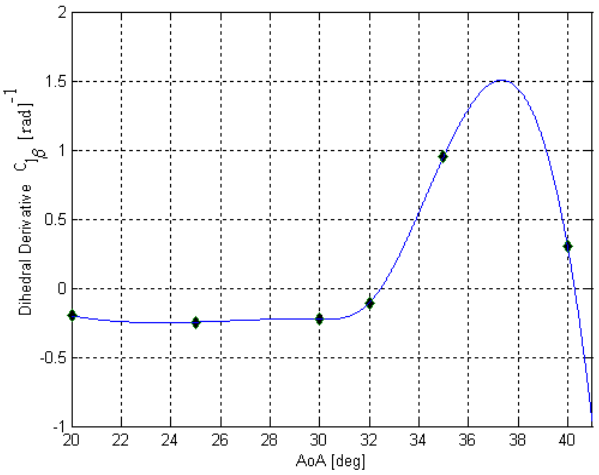

Fig. 14. Variation of the dihedral derivative C_{l_β} with angle of attack

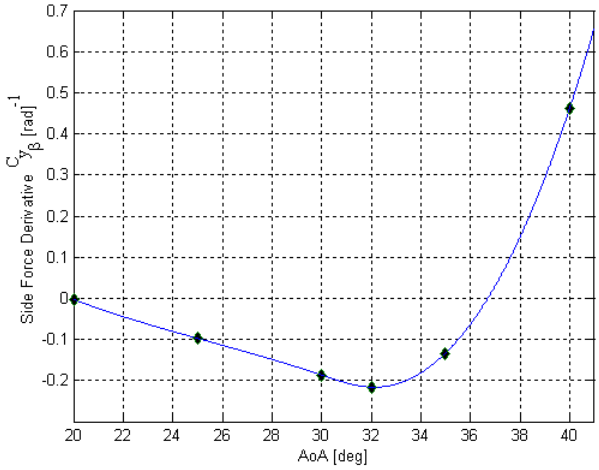

Fig. 15. Variation of the C_{y_β} -derivative with angle of attack

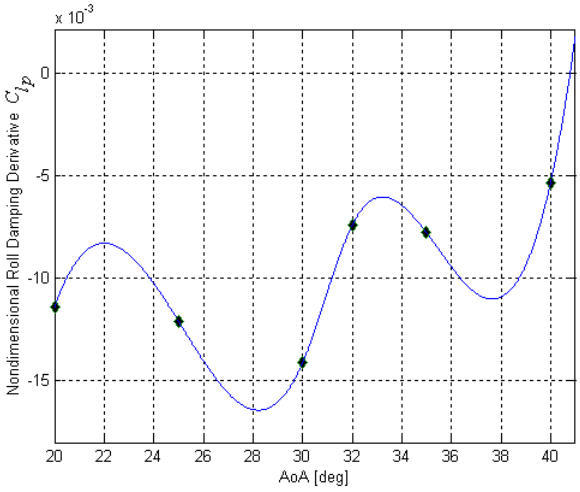

Fig. 16. Variation of the damping-in-roll derivative, C_{l_p} , with angle of attack

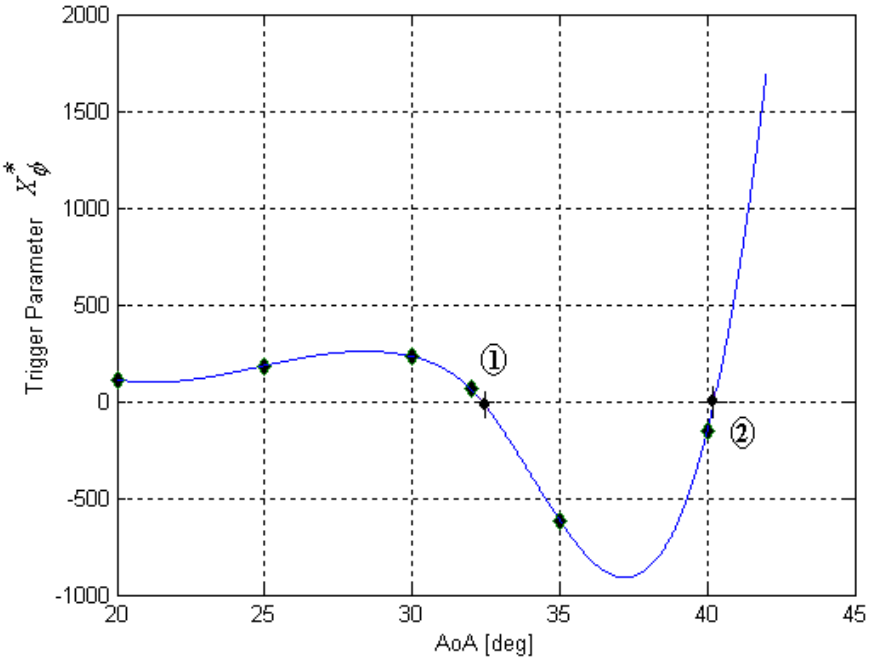

Fig. 17. Variation of the trigger parameter X_φ with angle of attack

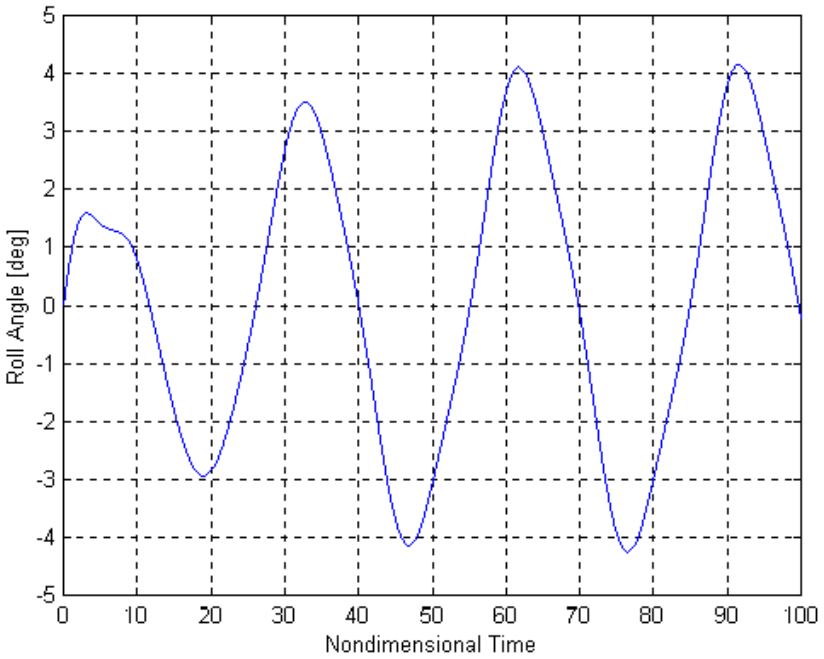

Fig. 18. Roll angle response due to the excitation of wing rock
in three degrees-of-freedom at $\alpha = 40^o$

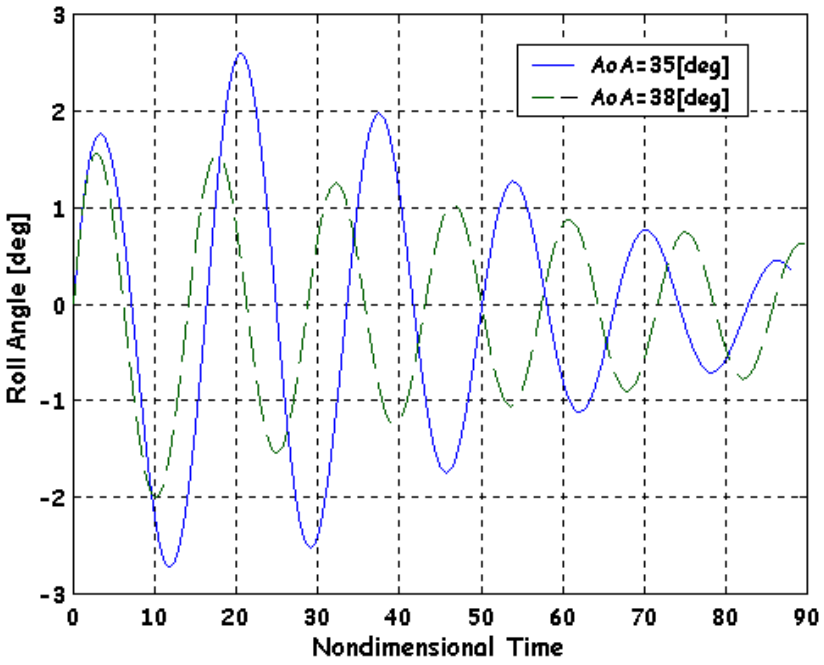

Fig. 19. Roll angle responses due to the excitation of wing rock in three degrees-of-freedom at $\alpha = 35^{o}$ and 38^{o}.